JGR Atmospheres

RESEARCH ARTICLE
10.1029/2024JD043054

Vertical Velocity and Diabatic Heating Top-Heaviness in the Convective Evolution Over Tropical Oceans

Yi-Chien Chen[1] and **Hirohiko Masunaga**[2]

[1]Graduate School of Environmental Studies, Nagoya University, Nagoya, Japan, [2]Institute for Space-Earth Environmental Research, Nagoya University, Nagoya, Japan

Key Points:

- Top-heaviness of vertical velocity and diabatic heating follows the typical life cycle of a mesoscale convective system
- Shallow mode contributes more significantly to eastern Pacific and Atlantic Ocean, whereas western Pacific and Indian Ocean are primarily dominated by the deep convective mode
- The contribution of convective modes varies with different rain types

Correspondence to:
Y.-C. Chen,
chen.yi.chien.s8@f.mail.nagoya-u.ac.jp

Citation:
Chen, Y.-C., & Masunaga, H. (2025). Vertical velocity and diabatic heating top-heaviness in the convective evolution over tropical oceans. *Journal of Geophysical Research: Atmospheres*, *130*, e2024JD043054. https://doi.org/10.1029/2024JD043054

Received 27 NOV 2024
Accepted 12 SEP 2025

Author Contributions:
Conceptualization: Yi-Chien Chen
Formal analysis: Yi-Chien Chen
Investigation: Yi-Chien Chen
Methodology: Yi-Chien Chen, Hirohiko Masunaga
Supervision: Hirohiko Masunaga
Validation: Yi-Chien Chen
Visualization: Yi-Chien Chen
Writing – original draft: Yi-Chien Chen
Writing – review & editing: Yi-Chien Chen, Hirohiko Masunaga

Abstract Convective heating and vertical motion are closely linked to each other and follow similar evolutionary paths over their convective life cycle. It has not yet been extensively explored, using observation, how such a collaborative evolution changes systematically from region to region over tropical oceans. In this study, the ERA5 reanalysis data and satellite measurements from Tropical Rainfall Measuring Mission Precipitation Radar are analyzed to examine the variability of the large-scale vertical velocity (ω) and diabatic heating (Q_1) profiles over tropical oceans. Hour-to-hour variability in these variables is examined based on composite time series to delineate the evolution of ω and Q_1 before and after Global Satellite Mapping of Precipitation (GSMaP) precipitation peaks. Four tropical basins are selected to study regional differences: western Pacific (WP), eastern Pacific (EP), Indian Ocean (IO), and Atlantic Ocean (AO). The composite time series reveal that the ω and Q_1 distributions align with the typical life cycle of mesoscale convective systems (MCSs). Empirical orthogonal function (EOF) decomposition is applied to the vertical structure of ω and Q_1 in terms of top-heaviness. The ω and Q_1 top-heaviness ratio (THR) delineate similar evolutionary curves in that THR enhances as convection intensifies, but the peak hour occurs earlier for Q_1 by several hours than for ω. The top-heaviness of ω and Q_1 exhibits a notable regionality that they are bottom-heavier in EP and AO than in WP and IO. Different rain types of shallow, deep convective, and stratiform are closely related to specific empirical orthogonal function modes in a regionally independent manner.

Plain Language Summary Moisture and heat are transported from the lower atmosphere to the mid-to-upper levels through upward motion, eventually resulting in precipitation. The vertical structure of air motion and of the cloud-induced heating plays a key role in the development of convection as it shapes the processes of the convective life cycle. However, the impact of the vertical structure on convective development can vary across different regions. This study explores how the vertical structure of vertical velocity and heating evolve during convection and how these processes vary over tropical oceans. We detail from global observations the way in which the evolution of convection is driven by the combined effects of vertical velocity and heating. The vertical structure of both velocity and heating follows the typical life cycle of convective systems. These vertical structures show distinct regional characteristics, although different types of heatings remain consistent across regions. This work provides new insights into tropical convection, especially in understanding the role of heating. Further studies are essential to clarify the mechanisms driving these regional differences.

1. Introduction

A complex interplay between thermal energy and moisture is involved in the interactions between tropical convection and the large-scale environment in global weather and climate (Kuo et al., 2018; Maloney et al., 2019; Neelin & Held, 1987; Wolding et al., 2020). The thermodynamic effects of moist convection on the atmospheric column vary with vertical motion itself (Back & Bretherton, 2006; Bui et al., 2016; Chen & Yu, 2021; Inoue & Back, 2015). The vertical motion and the diabatic heating profiles are related to each other thermodynamically in terms of the dry static energy (DSE) budget (Handlos & Back, 2014; Yanai et al., 1973). In the tropics, a large Rossby radius of deformation allows gravity waves to redistribute a temperature perturbation rapidly, making temporal and horizontal variations stay minimal (Bretherton & Smolarkiewicz, 1989; Charney, 1963; Sobel & Bretherton, 2000). Consequently, the primary balance in the energy budget lies between the vertical DSE advection and the apparent heat source (Q_1), indicating that the vertical profile of diabatic heating is closely related to the vertical motion profile. The interplay of heating and large-scale vertical motion has been extensively studied in the literature (Back & Bretherton, 2006; Hartmann et al., 1984; Huaman & Schumacher, 2018; Inoue & Back, 2017; Schumacher et al., 2004; Wu et al., 2000). However, fundamental questions remain regarding the

physical factors controlling the vertical profiles of heating and vertical motion, including the microphysical processes, environmental moisture, and dynamic forcing each affecting the vertical profiles (Back et al., 2017; Hagos et al., 2010; Marinescu et al., 2016). In addition, recent studies have highlighted regional and temporal variability in the heating profiles (Ahmed et al., 2016; Huaman & Schumacher, 2018; Tao et al., 2006), raising further questions about how such variability affects large-scale circulations and feedbacks to convection. The accuracy and consistency of latent heating retrievals from different satellite products also remain an ongoing challenge (Masunaga, 2013; L'Ecuyer & McGarragh, 2010). Despite recent advances in our understanding of heating, the factors controlling the vertical distribution of diabatic heating and its interaction with vertical motion remain unresolved in tropical meteorology.

Variations in the heating profile affect atmospheric circulations and influence the distribution of tropical rainfall (Hartmann et al., 1984; Schumacher et al., 2004; Wu et al., 2000). Past research employed observed heating profiles from mesoscale convective systems (Mapes & Houze, 1995; Schumacher et al., 2004) or idealized profiles of large-scale diabatic heating (Geisler, 1981; Hartmann et al., 1984; Wu et al., 2000) to explore the heating of moist convection. Since different precipitation systems produce distinct heating profiles (Schumacher et al., 2008; Sherwood et al., 2014), understanding how tropical rainfall affects large-scale circulation is crucial. Previous studies have also identified two leading modes of heating: the deep mode and the shallow mode, which account for the majority of the heating variability (Chen & Yu, 2021; Takayabu et al., 2010; Zhang & Hagos, 2009). The vertical structure of heating evolves significantly throughout the convective life cycle, exerting important influences on both the mesoscale and large-scale circulation. Previous studies have examined that the convectively suppressed phase is characterized by low-level heating associated with shallow convection, while the active phase exhibits a distinctive double-peaked heating profile related to midlevel convection and stratiform precipitation (Barnes et al., 2015; Funk et al., 2013; Johnson et al., 1999; Schumacher et al., 2004). As the convective stage gives way to the stratiform stage, the vertical evolution of heating plays a critical role in modulating upper-level divergence and influencing large-scale circulation. The fidelity of the vertical structure of heating simulated in numerical models is yet to be verified, while accurately reconstructing the heating from observations remains a challenge, despite the known importance of further understanding tropical convection and its interactions with large-scale atmospheric dynamics (Chikira, 2014; Jiang et al., 2015; Schumacher et al., 2004).

Additionally, vertical motion profiles are known to exhibit significant regional differences. In the western Pacific (WP), the vertical motion profile is climatologically top-heavy, while it tends to display a bottom-heavy structure in the eastern Pacific (EP) (Back & Bretherton, 2006; Back et al., 2017; Bernardez & Back, 2024; Bui et al., 2016; Trenberth et al., 2000; Zhang et al., 2004). Satellite observations have revealed notable differences in precipitation characteristics between the WP and the EP. Shallow and stratiform precipitation are more frequent in the EP than the WP (Berg et al., 2002; Kubar et al., 2007; Nesbitt et al., 2006; Schumacher & Houze, 2003; Yokoyama & Takayabu, 2012). Chen and Masunaga (2024), hereafter CM24, further demonstrated the regionality of precipitation characteristics in these regions exhibit distinct evolutionary patterns depending on rainfall intensity. However, CM24 focused their analysis only on WP and EP without exploring the relationship of large-scale vertical motion with diabatic heating and how the heating profile varies over the convective life cycle. Nevertheless, the relationship between diabatic heating and large-scale vertical motion has not yet been systematically and regionally investigated. Further research is required to better quantify the vertical heating structures across different convections and regions, in order to advance our understanding of the regional characteristics of convective processes and the role of tropical convective evolution in shaping large-scale circulation.

This study aims to explore the regional variations of heating associated with the convective evolution by analyzing the diabatic heating and large-scale vertical motion during the tropical convective life cycle. The structure of this study is outlined as follows. Section 2 provides a description of the data utilized. Section 3 introduces the making of composite time series and the top-heaviness ratio (THR). Section 4 examines the vertical structure of large-scale vertical motion and diabatic heating varying with time during the convective life cycle. The findings are summarized in Section 5.

2. Data

In this study, a combination of reanalysis data and satellite measurements are analyzed to examine the variability of the large-scale vertical motion and diabatic heating profiles over tropical oceans. The Tropical Rainfall

Table 1
The Definition to Separate the Q_1 Profiles in Different Types From Tropical Rainfall Measuring Mission

Q1 types	TRMM PR rain type	Additional condition
Deep convective	Convective	stormTopHeight ≥ meltLevel
Stratiform	Stratiform	/
Shallow	Convective	stormTopHeight < meltLevel

Measuring Mission (TRMM) Precipitation Radar (PR) version 7 (the latest version at the time of this writing) spectral latent heating (SLH) product (Shige et al., 2004, 2007, 2009) is adopted for the diabatic heating $Q_1 - Q_R$ (Q1 minus QR). Here Q_1 is the apparent heat source and Q_R is radiative heating as defined more thoroughly in Section 3.1. In addition, Clouds and the Earth's Radiant Energy System—Synoptic Radiative Fluxes (CERES SYN1deg edition 4.1) product (Doelling et al., 2013, 2016) is used for the radiative heating rate at multiple levels. Because the TRMM SLH data set only provides $Q_1 - Q_R$ instead of Q_1 due to the inability to measure radiation from the TRMM instruments, multilayer radiative heating from CERES is incorporated to complement it. In the present study, $Q_1 - Q_R$ represents the diabatic heating from the TRMM data product, while Q_1 signifies the combination of TRMM and CERES data. We will provide a detailed definition of diabatic and radiative heating in Section 3.2. In addition, instantaneous Q_1 profiles are labeled as convective, stratiform, and shallow heating based on the TRMM PR rain-type flag, which is used later to separate the composite time series into different rain types. While both the convective and shallow cumulus types belong to the convective type, they are separated by an additional condition whether storm top height is higher or lower than the melting level (See Table 1). *It is worth noting* that although TRMM PR has limited sensitivity to weak and shallow precipitations (Nesbitt & Zipser, 2003; Schumacher & Houze, 2003), this does not mean that shallow precipitation are entirely missing in the TRMM PR measurements. Conversely, the TRMM SLH algorithm cannot recover undetected weak shallow precipitation and eventually characterize the whole spectrum of vertical latent heating profiles including shallow modes of convection (Shige et al., 2004, 2007; Takayabu et al., 2010). Takayabu et al. (2010) demonstrated that shallow convection accounts for a substantial fraction of the total latent heating over tropics when derived from TRMM SLH products.

Global Satellite Mapping of Precipitation (GSMaP) is a global precipitation data product developed by the Japan Science and Technology Agency (JST) and Japan Aerospace Exploration Agency (JAXA). The GSMaP algorithm internally makes use of information from the spaceborne radar measurements of precipitation from the TRMM and Global Precipitation Measurement (GPM) core satellites as the reference for passive microwave measurements. The GSMaP products include standard, real-time (NOW), near-real-time (NRT), and reanalysis (RNL) components with a high horizontal resolution ($0.1° \times 0.1°$) and hourly temporal resolution. Passive microwave measurements are further enhanced with the microwave-infrared (IR) combined algorithm (MVK) and the Gauge Correct Algorithm to achieve desired sampling frequency and accuracy. In this study, GSMaP Gauge RNL version 6 (Kubota et al., 2020) is utilized for identifying the local temporal maxima of surface rain to define composite time series as described later, taking advantage of the temporally and spatially continuous coverage of GSMaP unlike sporadic TRMM satellite overpasses.

The reanalysis atmospheric data are taken from the European Centre for Medium-Range Weather Forecasts (ECMWF) ERA5 product (Hersbach et al., 2020). ERA5 employs the integrated Forecasting System (IFS) Cy41r2 with the improved 4-dimensional variational analysis (4D-Var) data assimilation. Compared to its predecessor or ERA-Interim (Xu et al., 2022), ERA5 provides higher temporal and spatial resolutions and better alignment with satellite observational data. This work adopts the reanalysis variables for vertical motion (ω). Unlike single-orbit satellite data, reanalysis data offer a broader global coverage. ERA5 reanalysis data are matched to the TRMM satellite data to minimize the temporal and spatial sampling errors.

This study analyzes hourly data covering the 13-year period from 2001 to 2013, averaged horizontally to a common $1° \times 1°$ grid. Multilayer variables are adjusted to the ERA5 vertical resolution with 27 pressure levels from 1,000 to 100 hPa. The target analysis regions and locations are shown in Figure 1, which are western Pacific (WP), eastern Pacific (EP), Indian Ocean (IO), Atlantic Ocean (AO), and intertropical convergence zone (ITCZ). ITCZ is defined as the region where the climatological vertical pressure velocity at 500 hPa is less or equal to 0 ($\overline{\omega}_{500} \leq 0$, shown as the black shaded region in Figure 1). The target boxes for the analysis are specifically chosen to focus on regions with strong upward motion shown in Figure 1. The analysis results for ITCZ are used as the climatological reference of the whole tropical oceans.

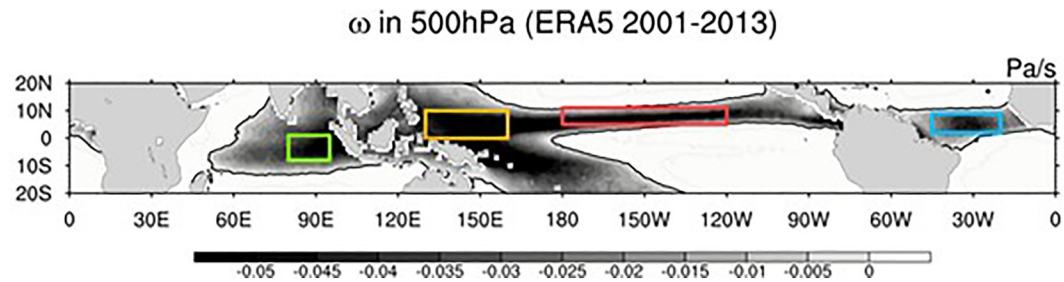

Figure 1. The spatial distribution of climatological vertical pressure velocity at 500 hPa ($\overline{\omega}_{500}$). The black solid curves showed the boundary of the ITCZ region, where the climatological vertical pressure velocity at 500 hPa is zero. The rectangular boxes mark the four target regions for analyzing the regional differences in precipitation composition, which include the western Pacific (WP) (0°–10°N/130°–160°E; yellow), eastern Pacific (EP) (5°–11°N/180°–120°E; red), Indian Ocean (IO) (8°S–1°N/80°–95°E; green), and Atlantic Ocean (AO) (2°–9°N/20°–45°E; blue).

3. Methodology

3.1. Composite Time Series

The hour-to-hour variability of convective processes is investigated by composite time series, in which instantaneous satellite measurements are averaged within an hourly bin sorted by the temporal lag/lead from the nearest precipitation maxima. A similar idea was employed originally proposed by Masunaga (2012, 2013) and Masunaga and L'Ecuyer (2014), combining measurements from multiple satellites in different orbits into a statistically continuous time series. This study follows the approach developed by CM24, that is, the satellite-observed and reanalysis parameters (ω and Q_1 in this case) are composited with respect to the local maxima of GSMaP rainfall. The detailed calculation procedures were thoroughly explained in CM24.

To identify the peak moment in the rainfall system evolution, a local maximum in GSMaP precipitation is defined as the peak value within a ±72 h time window in each 1° × 1° grid box. Time sequences collected around these local maxima from all grid boxes in the target regions are subsequently composited into a 144-hr time series with the local precipitation maximum anchored at time zero. Although the significant changes in convective cloud properties are usually observed between −12 and 12 h, a 144-hr window box was used for calculation to ensure comprehensive convective data, and the entire result was presented for completeness. Nevertheless, a smaller time domain as −18 to 18 h will be used in the figure of this study to provide a clearer view of the variations in a zoomed in version. Table 2 presents the number of 1° × 1° grids and the sample size of TRMM and ERA5 data sets for each region. The smaller sample number in the IO and AO regions is due to differences in the selection of the target domain. To ensure that all target boxes are located within areas of strong convective ascent (as shown in Figure 1), the sizes of the selected regions vary accordingly. In addition, while both the precipitation and vertical motion data have a dense global coverage, the TRMM SLH data are more sporadic. To ensure the sampling consistency, we include both Q_1 and ω only where TRMM data are available. It is noted that a 5-hr running mean is applied in advance to GSMaP precipitation, TRMM diabatic heating, and ERA5 omega. Running mean is intended to reduce sampling noise that originates from different sources, including the sampling inhomogeneity in passive microwave (PMW) orbits ingested into the GSMaP algorithm and the intermittent nature of TRMM PR overpasses.

Table 2
The Number of Grids and the Sample Size in Each Region

	Regions			
	WP	EP	IO	AO
Number of 1° × 1° grid	250	360	105	175
TRMM case number	6,790	7,765	2,900	3,309
ERA5 case number	234,265	284,363	99,997	120,158

3.2. Heating Formulation

In atmospheric thermodynamics, the total heating rate (Q) represents the combined effects of all heat sources within an atmospheric column, including solar radiation, surface sensible heat flux, latent heat release, and other processes influencing temperature changes. These heating mechanisms collectively regulate convective activity and the development of weather systems. More specifically, apparent heating source Q_1 summarizes the diabatic sources of heating, primarily consisting of latent heat release from condensation and radiative heating, reflecting the impact of convection on atmospheric heat budgets. Apparent heating source Q_1 was defined by Yanai et al. (1973) as

$$Q_1 \equiv \frac{\partial \overline{s}}{\partial t} + \overline{\nabla \cdot s\boldsymbol{V}} + \frac{\partial \overline{s\omega}}{\partial p} = Q_R + L(c-e) + Q^s_{\text{turb}} \tag{1}$$

where s is DSE, defined as $s = C_pT + gz$, C_p is the atmospheric specific heat at constant pressure, gz is geopotential, ω is vertical pressure velocity, L is the specific latent heat of condensation, c is the condensation rate, and e is the evaporation rate. In this expression, the overbar ($\overline{\ }$) denotes the time mean based on hourly data.

The term Q^s_{turb} can be also shown as

$$Q^s_{\text{turb}} = -\nabla \cdot \overline{s'\mathbf{v}'} - \frac{\partial}{\partial p}\overline{(s'\omega')} \tag{2}$$

This term represents the eddy transport of heating in the DSE budget, which can redistribute DSE by unresolved eddies. The prime ($'$) represents the deviation from hourly data time mean, corresponding to the perturbation component of each variable.

Radiative heating, Q_R, consists of shortwave radiation $(Q_R)_{SW}$ and longwave radiation $(Q_R)_{LW}$ as follows:

$$Q_R = (Q_R)_{SW} + (Q_R)_{LW} \tag{3}$$

where

$$(Q_R)_{SW} = \left(SW^{\downarrow} - SW^{\uparrow}\right) \tag{4}$$

$$(Q_R)_{LW} = \left(LW^{\downarrow} - LW^{\uparrow}\right) \tag{5}$$

where SW and LW represent shortwave and longwave radiation. The superscripts "↓" and "↑" denote downward and upward components. Shortwave radiation originates from solar radiation, resulting in a pronounced diurnal cycle. In contrast, longwave radiation is emitted by both the Earth's surface and the atmosphere itself in the form of infrared radiation.

As mentioned in the Chapter 2, the TRMM SLH data set does not contain radiative heating but instead provides $Q_1 - Q_R$, so we incorporated the radiative heating from CERES to complement the Q_1: as follows:

$$Q_1 = (Q_1 - Q_R)_{\text{TRMM}} + (Q_R)_{\text{CERES}} \tag{6}$$

where $(Q_1 - Q_R)_{\text{TRMM}}$ represents the diabatic heating from the TRMM data product, while $(Q_R)_{\text{CERES}}$ denotes the multilayer radiative heating obtained from the CERES data set. The term Q_1 incorporates information from both TRMM and CERES data. In the presence of intense convection, Q_1 is largely contributed by latent heating with the radiative heating Q_R being smaller. Nevertheless, we retain Q_R from CERES to make up $(Q_1 - Q_R)_{\text{TRMM}}$ in this study for theoretical completeness.

3.3. Top-Heaviness Ratio

Back et al., 2017 (hereafter BH17) introduced THR as a practical measure of the structural characteristics of vertical motion. As the ratio of the first and second vertical modes as obtained from the empirical orthogonal functions (EOFs) (e.g., Back & Bretherton, 2009; Back et al., 2017; Chen & Yu, 2021), THR is a useful parameter clearly summarizing the geographic variability in the vertical structure of vertical motion. We follow BH17 in defining the THR of vertical motion, but here, THR is also applied to the TRMM diabatic heating profiles. The vertical pressure velocity, ω, and diabatic heating, Q_1, are assumed to be well approximated by the first two principal components as follows:

$$\omega(p,t) \approx a_1(t)\Omega_{\omega 1}(p) + a_2(t)\Omega_{\omega 2}(p) \tag{7}$$

$$Q_1(p,t) \approx b_1(t)\Omega_{Q_1 1}(p) + b_2(t)\Omega_{Q_1 2}(p) \tag{8}$$

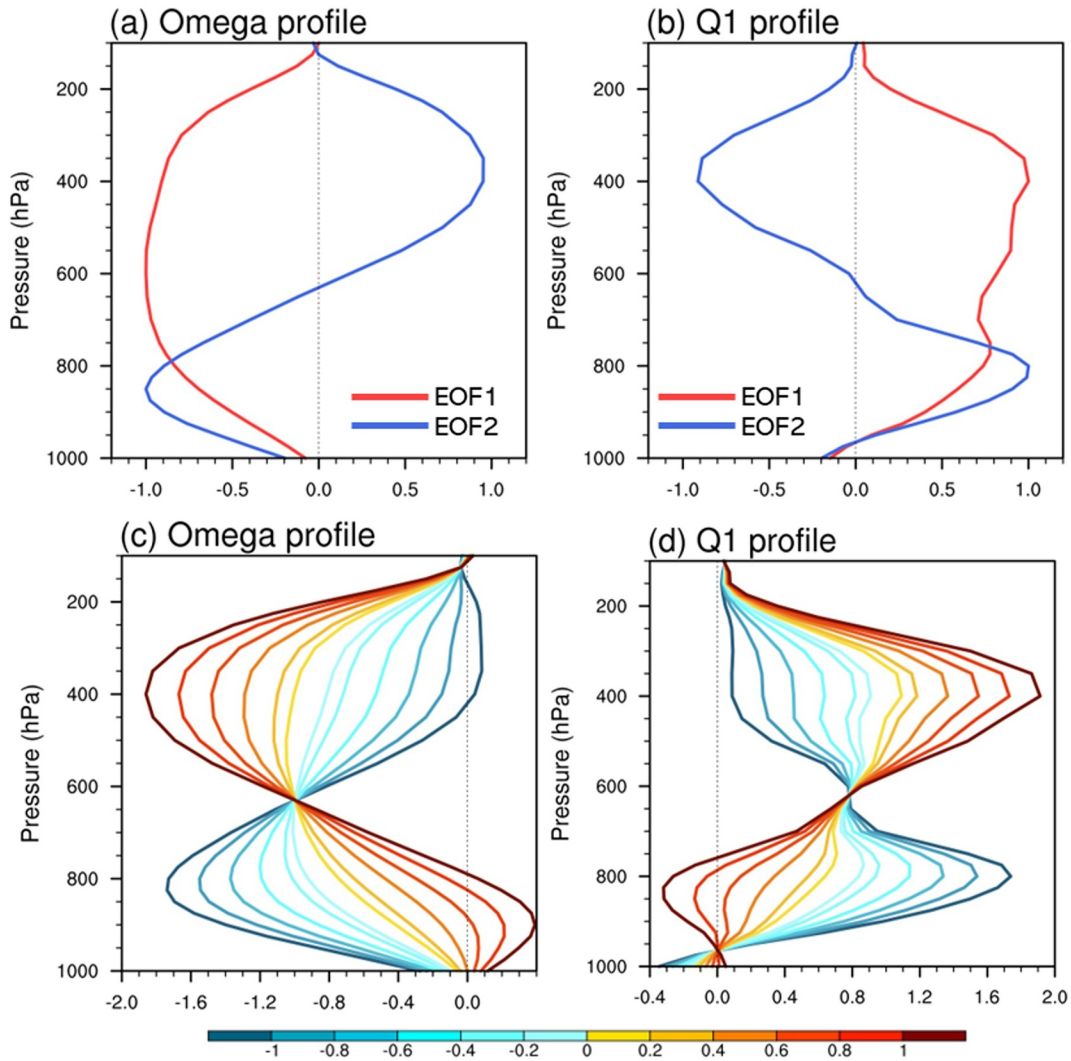

Figure 2. The first and the second empirical orthogonal function modes (Ω_1 in red solid line and Ω_2 in blue solid line) of (a) vertical motion (ω) form reanalysis data and (b) diabatic heating (Q_1) form Tropical Rainfall Measuring Mission observation data. Reconstruction of the vertical profile of (c) vertical motion and (d) diabatic heating with a range of top-heaviness ratio.

where $\Omega_{\omega i}$ and $\Omega_{Q_1 i}$ are the ith EOF of the vertical profile of ω and Q_1 ($i = 1, 2$), respectively. These EOFs are calculated individually for ω and Q_1 from all hourly $1^\circ \times 1^\circ$ samples across the entire ITCZ. The values a_i and b_i are the ith principal component, representing the magnitude of each vertical mode.

Figures 2a and 2b shows the first two EOF modes profile of the ω ($\Omega_{\omega 1}$ and $\Omega_{\omega 2}$) and Q_1 ($\Omega_{Q_1 1}$ and $\Omega_{Q_1 2}$) in the ITCZ. The first and second EOFs explain 63% and 18.6%, respectively, of the total variance in ω and 73.7% and 17.7% of the total variance in Q_1. Note that each curve in Figures 2a and 2b has been normalized by the maximum value. EOF1 represents the vertical motion or heating effect to the atmospheric column extending throughout the entire troposphere, while EOF2 depicts an updraft/downdraft pair or a heating/cooling pair that changes its sign near the midtroposphere. A positive EOF1 is defined as an updraft of ω and a heating of Q_1, similar with a deep convective cloud structure; whereas a negative EOF1 describes the opposite structure with a downdraft of ω and a cooling of Q_1. A positive EOF2 is defined as a low-level updraft of ω, an upper-level downdraft, a low-level heating, and an upper-level cooling of Q_1, creating a shallow cloud structure. Conversely, a negative EOF2 has a lower downdraft (cooling) and an upper updraft (heating), typical of the stratiform cloud structure.

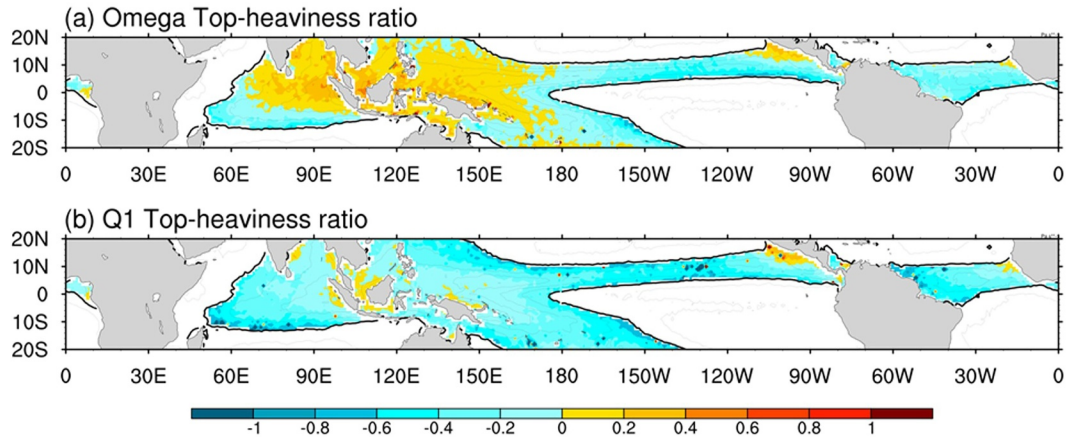

Figure 3. The climatological spatial distribution of (a) the ω top-heaviness ratio (THR) and (b) Q_1 THR in the ITCZ region. The color shaded represents the vertical profile as the same as Figures 2c and 2d, respectively.

Combining EOF1 and EOF2 with different values of THR, a sequence of different vertical structures of ω and Q_1 are reconstructed as demonstrated in Figures 2c and 2d.

After obtaining the EOFs from the ITCZ region, the principal components are derived by projecting the first two EOFs to the raw time series of ω and Q_1 at each tropical grid point as follows:

$$\omega(x,y,p,t) = a_1(x,y,t)\Omega_{\omega 1}(p) + a_2(x,y,t)\Omega_{\omega 2}(p) \tag{9}$$

$$Q_1(x,y,p,t) = b_1(x,y,t)\Omega_{Q_1 1}(p) + b_2(x,y,t)\Omega_{Q_1 2}(p) \tag{10}$$

The THR of vertical motion and diabatic heating is calculated as

$$\omega_{\mathrm{THR}}(x,y,t) = -\frac{a_2(x,y,t)}{a_1(x,y,t)} \tag{11}$$

$$Q_{1\mathrm{THR}}(x,y,t) = -\frac{b_2(x,y,t)}{b_1(x,y,t)} \tag{12}$$

If the THR is positive, the vertical profile approaches a top-heavy structure. Conversely, the vertical profile tends to be bottom-heavy for a negative THR. Figures 3a and 3b show the climatological map of the ω THR and the Q_1 THR. Comparing Figures 2c and 2d with Figures 3a and 3b, the regional pattern of the climatological vertical profile of ω and Q_1 emerges itself. The ω THR is predominantly positive over the western Pacific warm pool, implying a top-heavy structure; on the other hand, Q_1 THR in the same region is overall weakly negative, suggesting that the heating structure tends to be modestly bottom-heavy. Both of ω THR and Q_1 THR show a zonal gradient with an overall decrease from the western to eastern Pacific, confirming the known regionality that vertical motion is climatologically more top-heavy in the WP than in the EP. Although the zonal gradient of Q_1 THR is less pronounced than that of ω THR, EP (Q_1 THR ≈ -0.3) still exhibits a shallower vertical heating structure than WP (Q_1 THR ≈ -0.1). The IO and AO are shown as top-heavy and bottom-heavy, respectively, in Figure 3a. The positive ω THR in WP and negative values in EP further confirm the dominance of deep convection in WP and of shallow convection in EP. However, the Q_1 THR exhibits weaker regional contrasts than the ω THR, which is an aspect that has not been explicitly quantified in earlier studies. These distinct spatial patterns in THR across different regions provide valuable insights into the regional characteristics of tropical convection.

It should be noted that the definition of the THR may influence the quantitative results, depending on the choice of basis modes. For instance, Hagos et al. (2010) employed rotated EOF (REOF) analysis, which yielded physically distinct modes representing deep and shallow convective heating structures as their first and second modes, respectively. In contrast, standard EOF analysis, as used in this study, produces orthogonal modes that are determined solely by statistical variance. As a result, the specific structure of the leading modes may vary

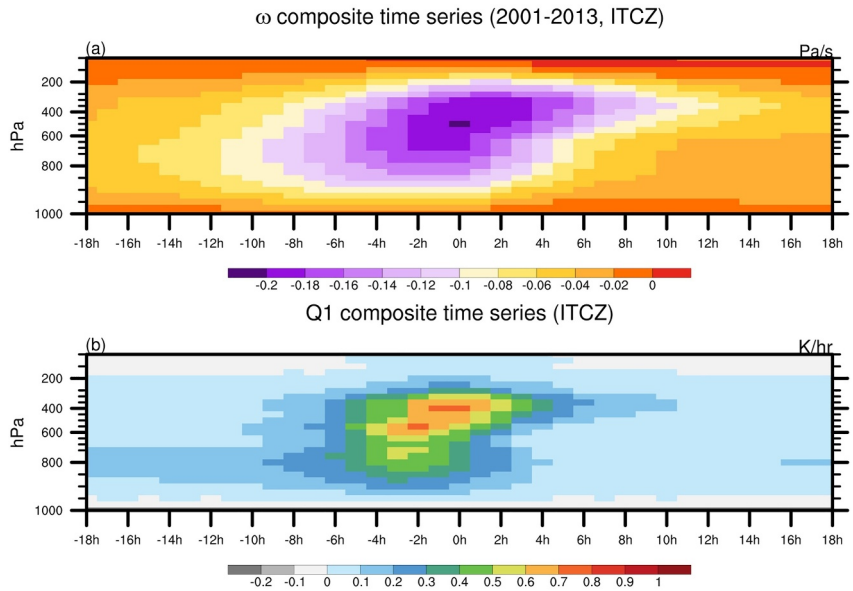

Figure 4. The vertical distribution of composite time series of (a) ω and (b) Q_1 in ITCZ.

depending on the decomposition method, which in turn can lead to subtle differences in the derived THR. For consistency across variables and to facilitate comparison between ω and Q_1, the standard EOF framework was adopted throughout this study.

4. Results

4.1. Evolution of ω, Q_1, and Q_R

Figure 4 depicts the composite time series of the vertical distribution of ω and Q_1. The tilted structures of ω and Q_1 during the convectively active period near time zero are reasonably explained by the known transition from shallow to deep convection and then to stratiform precipitation. This conforms the known mesoscale convective system (MCS) life cycle that the evolution of organized precipitating clouds such as MCSs accompanies a systematic development of internal cloud structure: shallow precipitation in the initial stage evolves into deep convective precipitation as an MCS is invigorated, followed by the expansion of stratiform precipitation from the mature to fading stages (Funk et al., 2013; Houze, 1989, 1997; Johnson et al., 1999; Kurowski et al., 2018; Lamer et al., 2015; Powell, 2016). The enhancement of Q_1 is more sharply confined over time than that of ω, as indicated by the enhancement of Q_1 between -8 and 8h, while ω is primarily distributed between -12 and 12h. The latent heating contained in Q_1 initially generates heating (at approximately -5 h, both the magnitude and the height of the maximum value in Q_1 begin to increase significantly) in the mid-to-upper atmosphere as latent heating release increases (Barnes et al., 2015; Chang & L'Ecuyer, 2019), while a strong vertical motion follows the increase of magnitude and peak height subsequently at around -2 h. This temporal lag between Q_1 and ω highlights a complex dynamical coupling between diabatic heating and vertical motion in tropical convective systems.

Figure 5 presents the composite time series of CERES radiation data, showing the vertical distribution of radiative heating throughout the convective life cycle. The original CERES radiation data consist of 6 vertical levels. To facilitate further analysis and calculation, the CERES radiation is linearly interpolated to 27 vertical levels, making its vertical resolution consistent with that of ERA5 and TRMM. The radiation cooling exhibits a modest enhancement around 0h and persists for several hours after reflecting the evolving cloud structure. The magnitude of Q_R is nonetheless quite small and has only minor influence on the overall conclusions drawn from the composite time series of Q_1.

4.2. Regional Variability of THR

To investigate the regional differences in the convective evolution of ω and Q_1 and the contributions of each EOF mode to these variables and regions, the principal component coefficients a and b from Equation 9 and

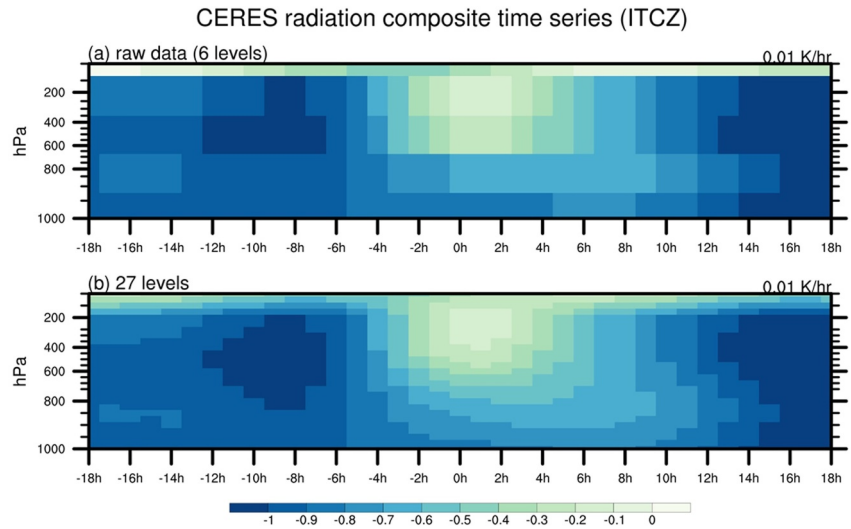

Figure 5. The vertical distribution of Q_R of (a) 6 levels (raw data) and (b) 27 levels in ITCZ. Note that the unit is 0.01 K/hr.

Equation 10 are extracted for each region. Figures 6a and 6b show the composite time series of the principal component coefficients a and b for the first mode, respectively. The first mode stays positive and a notable enhancement around time zero, indicating a vertically penetrating updraft and heating within the atmospheric column that strengthens as convection develops. In terms of regionaility, the first mode of ω exhibits a notably higher amplitude in EP, with the peaks occurring later in both EP and the AO than other regions. The convective systems in EP and AO are generally shallower and display a bottom-heavy structure (as shown in Figure 3a). These regions are known to have lower sea surface temperatures than WP and IO, which may be among the factors hindering convection from quickly deepening. This results in a higher amplitude and a delayed peak of the first mode of ω in these regions. Additionally, the first mode of Q_1 follows qualitatively similar evolutionary paths across all regions but with a higher amplitude in WP, IO, and AO than EP.

Figures 6c and 6d present the composite time series of coefficients a and b for the second mode. During the convectively active period (−12–12 h), the second mode coefficients of ω and Q_1 both first increase until they reach a positive peak, followed by a decrease to a negative value before tapering off. The initial rise to a maximum corresponds to shallow convection (updraft and heating in the lower levels and downdraft and cooling in the upper levels) and the following minimum may be interpreted as stratiform precipitation (downdraft and cooling in the lower levels and updraft and heating in the upper levels). This pattern resembles the typical life cycle of an MCS. During the convection inactive period (−18 to −8 h), the second-mode contribution to ω in the WP and IO in Figure 6c is almost zero, while those to Q_1 are positive in all regions in Figure 6d. This indicates the relative dominance of the first mode even outside the convectively active spell in the WP and IO, in contrast to the EP and AO where the shallow mode retains a persistent contribution to the regional climatology.

The THR is calculated with Equation 11 and Equation 12, which provides a clearer interpretation of the vertical structure. Figure 7 shows the composite time series of the ω THR and Q_1 THR. Both THRs share a similar evolutionary curve with an enhancement as convection intensifies, but with a distinct time lag in the peak hour. The Q_1 THR reaches the peak right on time zero or slightly after, followed by the ω THR peaking 5–6 hr later. The ω THR (solid line) and Q_1 THR (dashed line) exhibit higher values in the WP and IO than in the EP and AO throughout the evolution. This indicates that both ω and Q_1 have a shallower structure in the EP and IO than in the WP and IO, conforming the previous studies showing that EP has a more bottom-heavy vertical structure and shallower precipitation than the WP (Back & Bretherton, 2006; Chen & Masunaga, 2024; Huaman et al., 2022; Zhang et al., 2004). The ω THR reaches a higher peak than the Q_1 THR in WP and IO, which can also be seen in Figure 3. On the other hand, the peak values are similar between the ω THR and the Q_1 THR in EP and AO. Q_1 tends to be more concentrated in the lower troposphere than ω, even in deep convective regions, resulting in a weaker bottom-heavy signal in the Q_1 THR than in the ω THR in the WP and IO regions. In contrast, both the Q_1 THR and ω THR exhibit a similar bottom-heavy structure in the EP and AO regions. The differences in the

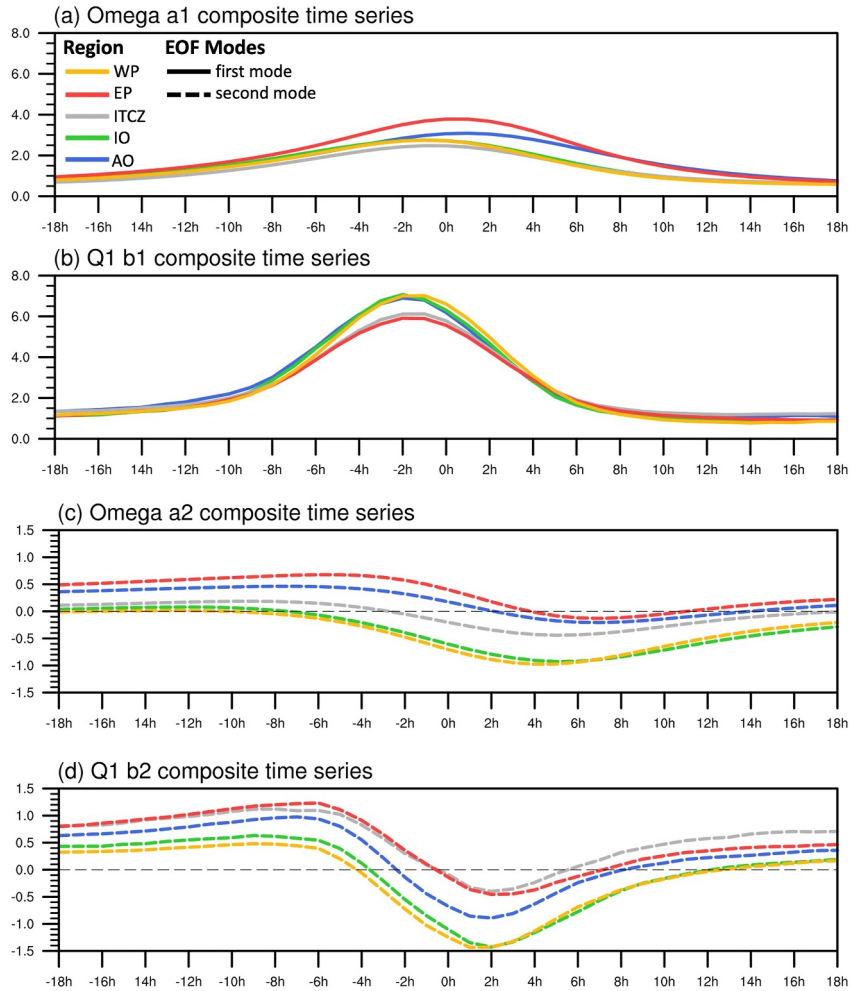

Figure 6. The principal component value of the composite time series in each region of (a) $\omega\, a_1$ and (b) $Q_1\, b_1$ in the first mode (solid line) and (c) $\omega\, a_2$ and (d) $Q_1\, b_2$ in the second mode (dash line).

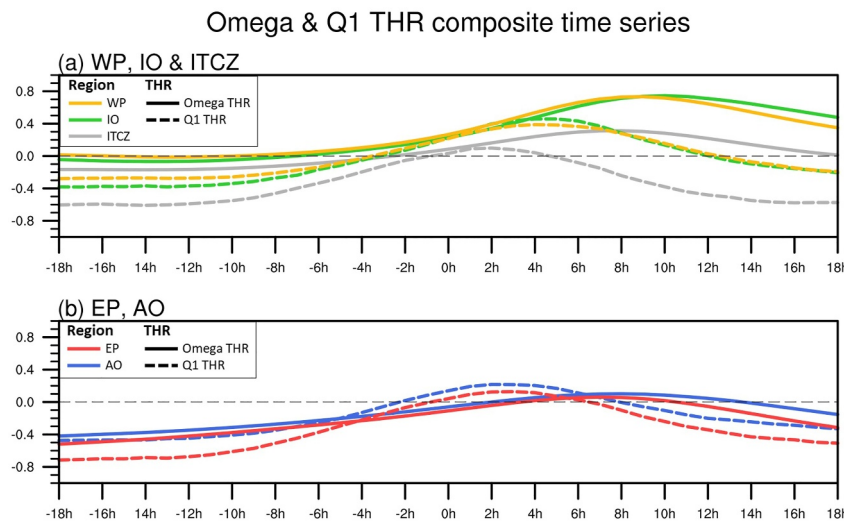

Figure 7. Composite time series of the ω top-heaviness ratio (THR) (solid line) and Q_1 THR (dash line) in panels (a) WP and IO and (b) EP and AO with the reference of ITCZ.

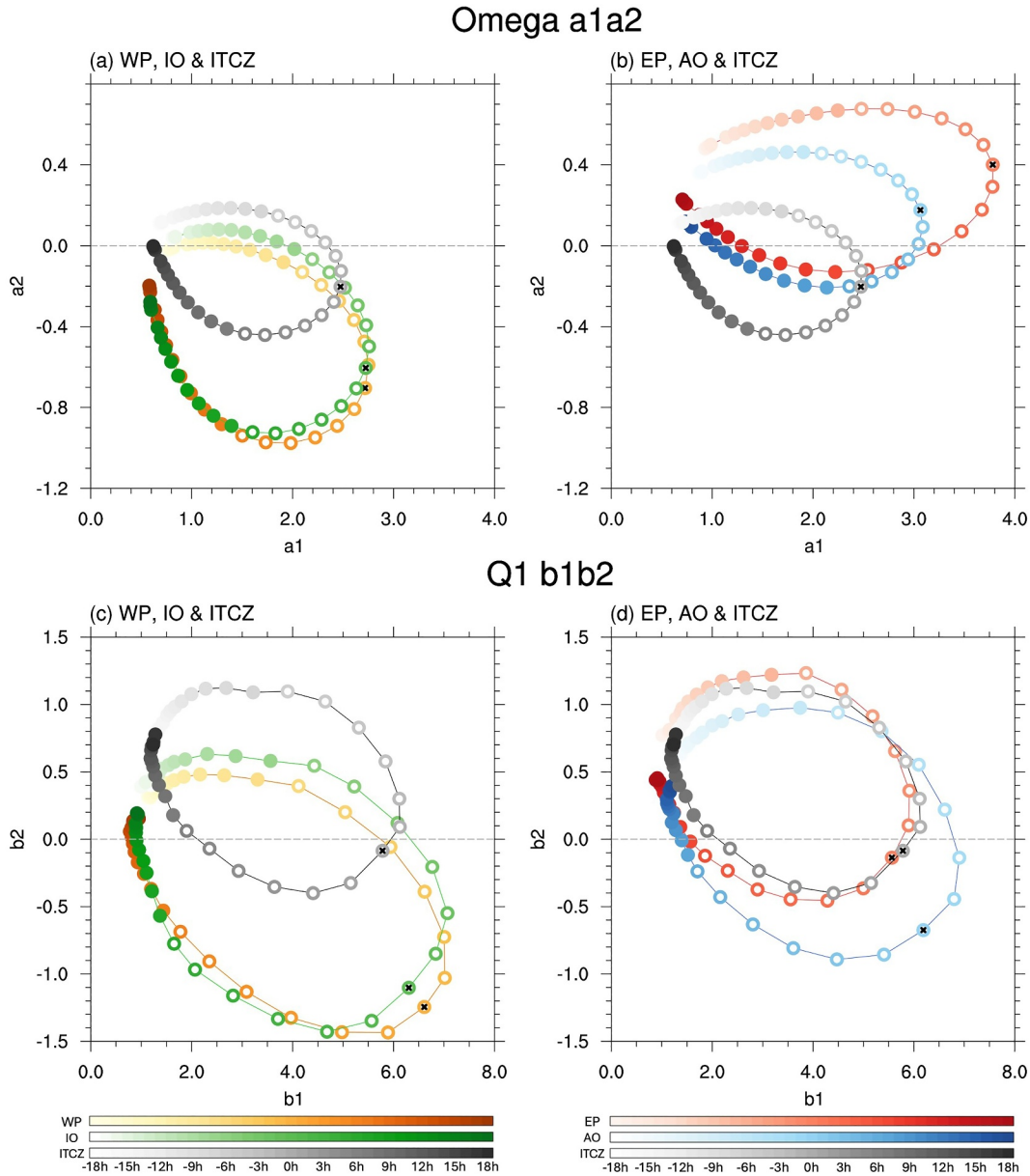

Figure 8. Shown Figure 6 as the scatterplot. The first mode and second mode principal component values of ω in panels (a) WP and IO and (b) EP and AO and the result of Q_1 in panels (c) WP and IO and (d) EP and AO with the reference of ITCZ during ±18 h. The life cycle progression follows a clockwise direction in the figures. The black cross indicates the time point at 0h, and the hollow dots emphasize the period between −6 and 6 h.

vertical gradient between ω and Q_1 across these regions help to explain the observed variations in the peak values of the ω THR and Q_1 THR.

Figure 8 presents the phase-space diagram between the first and second principal components focusing on the results within ±18 h in Figure 6. In the diagram, the trajectories of both ω and Q_1 appear in the same order: EP, AO, IO, and WP from the top to the bottom. The EP and AO have a larger value of the second mode (more bottom-heavy), whereas the WP and IO exhibit a consistently negative value of the second mode (more top-heavy). The finding aligns with previous studies that reported a higher rain fraction of shallow and stratiform convection in the EP (Berg et al., 2002; Back et al., 2017; Schumacher & Houze, 2003; Yokoyama & Takayabu, 2012).

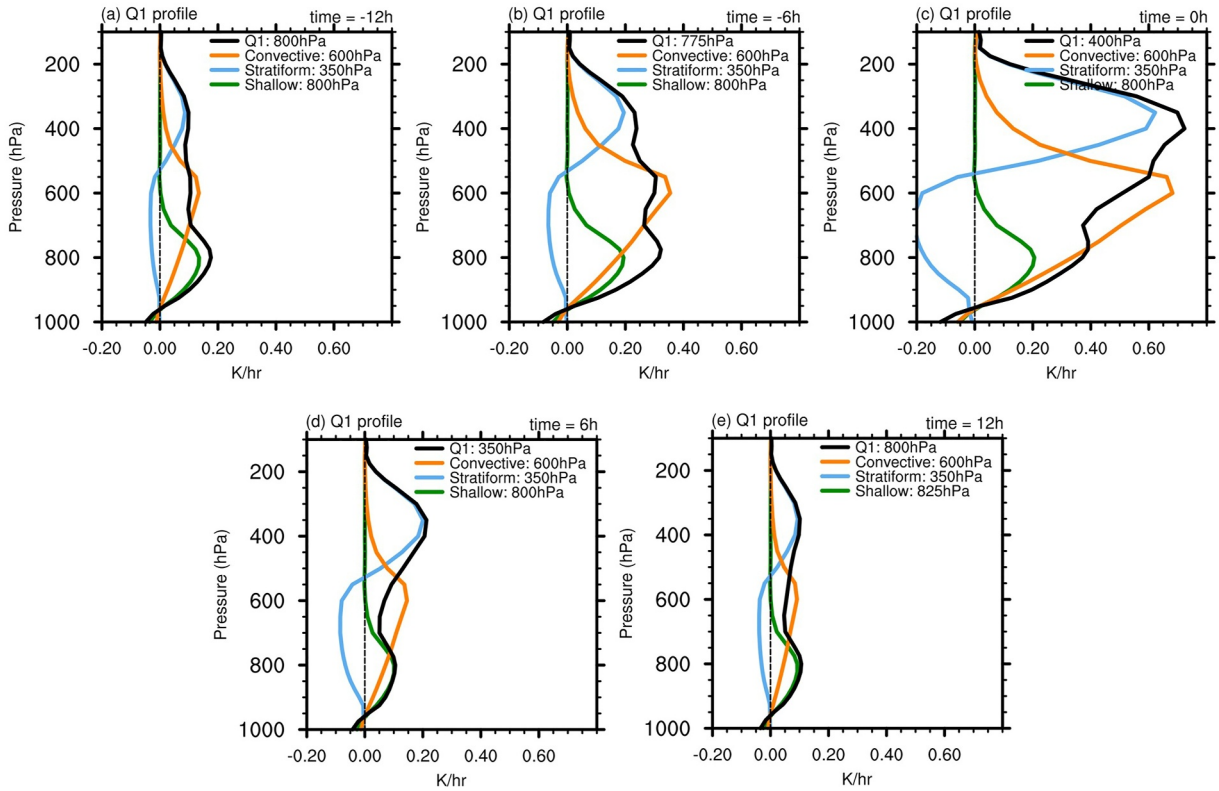

Figure 9. The Q_1 vertical profile of Figure 4 in deep convective, stratiform, and shallow types at (a) −12 h, (b) −6 h, (c) 0 h, (d) 6 h, and (e) 12 h. The black solid line showed the vertical profile of Figure 4 or the combination of deep convective, stratiform, and shallow Q_1. The pressure levels in the legend refer to the heights of the vertical profiles.

4.3. Regionality of Q_1 in Different Types

The systematic evolution of Q_1 is attributed to a transition from shallow to deep convection and then to stratiform rain. To confirm this, the composite time series of Q_1 is further decomposed into deep convective, stratiform, and shallow types using the TRMM PR rain-type flag. Figure 9 presents selected snapshots of the decomposed vertical profiles from −12 to +12 h taken from the original time series in Figure 4b. Shallow, stratiform, and deep convective Q_1 each have a peak at 800, 350, and 600 hPa, respectively. In an early stage of convective development (−12 h), the three types have a comparable magnitude of heating, with the shallow heating responsible for the bottom-heavy structure of total Q_1. As the evolution enters the active phase, deep convective Q_1 and stratiform Q_1 show a significant enhancement in magnitude, leading to a relatively top-heavy Q_1 structure. In a later stage of convective development (6 h), deep convective Q_1 rapidly dissipates, establishing an even top-heavier structure dominated by stratiform Q_1. Eventually, a convectively quiet state returns where the strengths of the three rain types are approximately the same as one another. Throughout the entire convective development processes, shallow Q_1 remains barely enhanced from the background, with its intensity changes not as strikingly as the other two types. Both deep convective Q_1 and stratiform Q_1 exhibit a noticeable enhancement, causing a transition in structure from bottom-heavy to top-heavy. It follows that the total Q_1 profile has a weak peak at around 800 hPa during hours outside the convectively active period, while the peak starts rising rapidly at approximately −6 h until it reaches 350 hPa at 12 h. After 12 h, convection quickly diminishes in amplitude with a faint peak lingering at 800 hPa. The transition from a bottom-heavy to a top-heavy structure is consistent with previous studies describing the development of organized tropical convective systems, which typically begin with shallow convection driven by low-level heating and gradually deepen into deep convective and stratiform clouds (Inoue & Back, 2015; Lappen & Schumacher, 2012, 2014; Mapes et al., 2006; Takayabu et al., 1996). The evolution of convection associated with different vertical structures also leads to distinct precipitation types at various stages of the convective life cycle (Houze, 1989, 1997; Kurowski et al., 2018; Mapes et al., 2006; Powell, 2016; Vogel

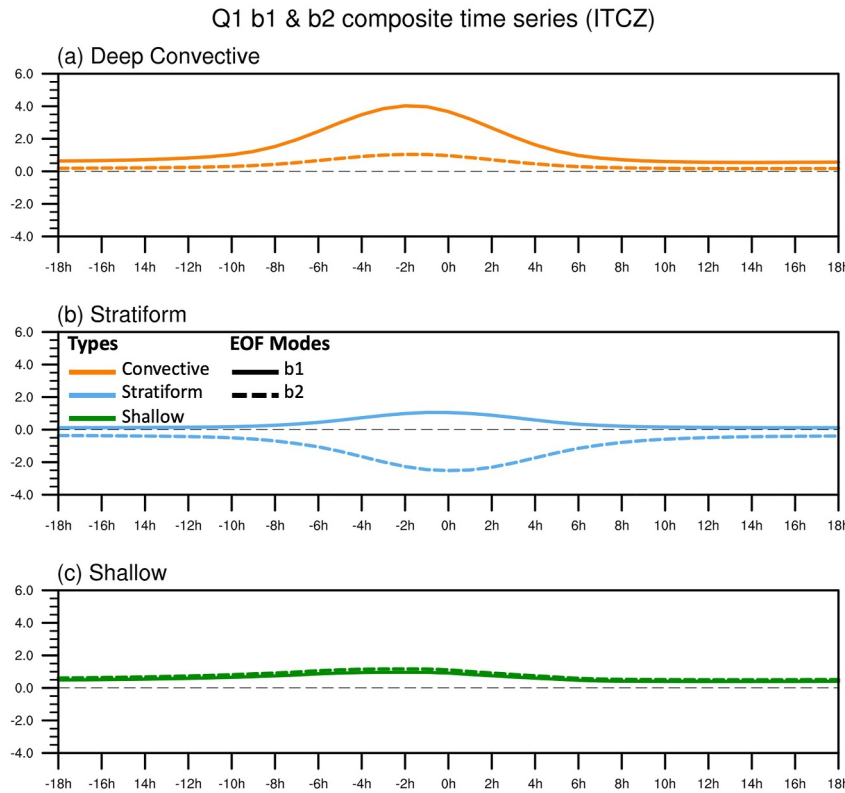

Figure 10. The composite time series as Figures 6c and 6d but in the (a) deep convective, (b) stratiform, and (c) shallow of Q_1.

et al., 2020; Zhang & Klein, 2010). This variation corresponds to the transition from bottom-heavy to top-heavy structures as convection develops over the topical ocean.

We next examine how the two EOF modes of Q_1 are related to the three rain types in the vertical structure. The deep convective, stratiform, and shallow Q_1 are decomposed as follows:

$$Q_1{}^{\mathrm{dconv}} = b_1{}^{\mathrm{dconv}}\Omega_{Q_1 1}(p) + b_2{}^{\mathrm{dconv}}\Omega_{Q_1 2}(p) \tag{13}$$

$$Q_1{}^{\mathrm{strat}} = b_1{}^{\mathrm{strat}}\Omega_{Q_1 1}(p) + b_2{}^{\mathrm{strat}}\Omega_{Q_1 2}(p) \tag{14}$$

$$Q_1{}^{\mathrm{shall}} = b_1{}^{\mathrm{shall}}\Omega_{Q_1 1}(p) + b_2{}^{\mathrm{shall}}\Omega_{Q_1 2}(p) \tag{15}$$

where $\Omega_{Q_1 1}$ and $\Omega_{Q_1 2}$ are the same as in Equation 8, representing the vertical profile patterns of the first and second EOF modes in the ITCZ. $Q_1{}^{\mathrm{dconv}}$, $Q_1{}^{\mathrm{strat}}$, and $Q_1{}^{\mathrm{shall}}$ refer to the deep convective, stratiform, and shallow Q_1, respectively, which are derived by decomposing Q_1 using the TRMM PR rain-type flag. b^{dconv}, b^{strat}, and b^{shall} are the principal component coefficients for different Q_1 types, obtained through EOF analysis.

Figure 10 shows the composite time series of the principal component coefficients for different Q_1 types in the ITCZ. The figure reveals that the leading mode for deep convective Q_1 is the first mode, while for stratiform Q_1, it is the second mode, as might be expected (Chen & Yu, 2021; Zhang & Hagos, 2009). In shallow Q_1, the first and second modes are comparable, indicating that both modes equally dominate the shallow type. The deep convective Q_1, dominated by positive EOF1, corresponds to a heating throughout the atmospheric column. On the other hand, the stratiform Q_1, accounted for primarily by negative EOF2, exhibits a low-level cooling and an upper-level heating. The balanced contributions of positive EOF1 and EOF2 in shallow Q_1 result in a heating confined to the lower troposphere.

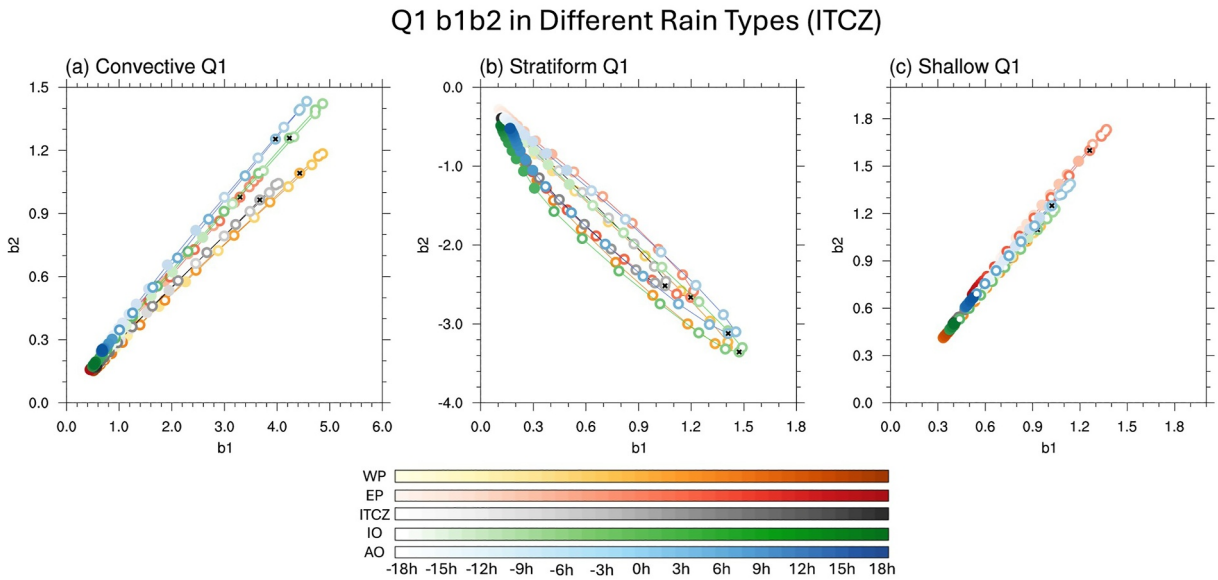

Figure 11. The scatterplot as Figure 8, but in the (a) deep convective Q_1, (b) stratiform Q_1, and (c) shallow Q_1 in ITCZ.

The regional differences among different Q_1 types are presented in the phase-space diagram in Figure 11. The convective and shallow Q_1 curves appear as near-straight lines, while the stratiform Q_1 curves follow an elongated oval path. For convective and shallow Q_1, no significant time lag is observed between the first and second modes, indicating that these heating profiles change in magnitude but are fixed in shape. In contrast, the stratiform Q_1 profile slightly changes in vertical structure toward the later stages of convection, where the lower levels gradually weaken and the upper levels deepen. During the convectively active period, the first mode still maintains slight heating in the middle and lower convective layers, resulting in a time difference between the peak values of the first and second modes for stratiform Q_1. Nevertheless, the curves for different Q_1 types overlap across different regions and do not show significant regionality unlike in Figure 8. The weak regionality may be due to assumptions built in the TRMM algorithm. The TRMM latent heating algorithm uses an internal lookup table consisting of reference heating profiles for each rain type that are regionally independent, which by design eliminate the potential regional variations in diabatic heating (Ling & Zhang, 2011; Shige et al., 2004).

5. Discussion

This study reveals a subtle but potentially important time lag between the top-heaviness evolution of Q_1 and ω during the convective life cycle. As shown in Section 4.2 and Figure 7, both Q_1 THR and ω THR increase as convection intensifies, but Q_1 THR reaches its peak at the time of peak rainfall or slightly after (0–2h), while ω THR peaks 5–6 hr later. This systematic delay suggests that the vertical structure of diabatic heating responds more promptly to convective development than the large-scale vertical motion.

To further explore the possible causes of the timing discrepancy between Q_1 THR and ω THR, Figure 12 presents the composite time series of Q_1 and each term in the DSE budget including vertical DSE advection, horizontal DSE advection, and the temporal tendency in vertical integration. Although the peaks of horizontal advection and temporal tendency occur at 5 and 6h, respectively, their magnitudes are smaller and thus unlikely to account for the observed time difference between Q_1 THR and ω THR. The vertical DSE advection, which is the primary contributor in the DSE budget, exhibits a temporal peak approximately 2 hours later than that of Q_1. This time lag may stem from intrinsic temporal inconsistencies between satellite-derived Q_1 and reanalysis-based ω. It is important to note that ERA5 is a model-assimilated reanalysis product and not a direct observation. As such, the timing of convective peaks derived from ERA5 may differ from satellite observations, particularly in the tropics where convective systems evolve rapidly. This limitation inherent of ERA5 is arguably a source of the inconsistency between vertical motion and diabatic heating as found in this study. Moreover, this discrepancy could be somewhat exaggerated in the THR. The top-heaviness ratio is a nonlinear combination of the first and second

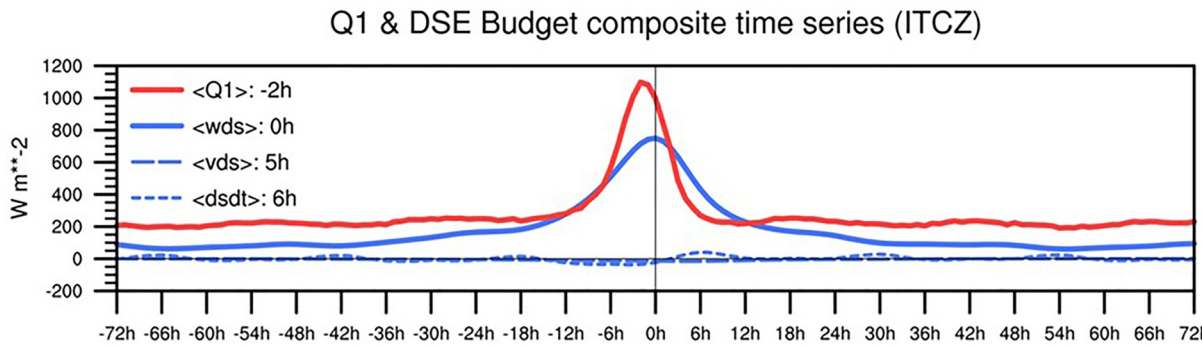

Figure 12. The composite time series of the vertical integral components in Q_1 and dry static energy (DSE) budget in ITCZ. The red curve represents Q_1 from satellite data; the blue curves are from ERA5 data in the units of W/m^2. The result of DSE budget is further shown as vertical DSE advection (blue solid curve), horizontal DSE advection (blue long dash curve), and time tendency (blue short dash curve). The time of each term indicated in the legend corresponds to the time points at which the maximum values occur.

modes. Even a small error residing in both the first- and second-mode time series could interact with each other in the calculation of THR, resulting in a more pronounced timing difference between the Q_1 THR and ω THR.

The results emphasize that while vertical motion and heating structures are closely tied, challenges remain to accurately estimate their time evolution from existing data sets. Future studies could further explore the physical mechanisms behind this lag using high-resolution cloud-resolving models or improved observational data sets with finer temporal sampling.

6. Conclusion

In this study, a combination of the ERA5 reanalysis data and satellite measurements from the TRMM PR SLH products are analyzed to examine the regionality and variability of the vertical structure of the large-scale vertical motion and diabatic heat over tropical oceans. GSMaP precipitation is utilized for identifying the local temporal maxima of surface rain to obtain the composite time series of vertical motion and heating for exploring the variations of variables associated with convective evolution.

The composite time series of vertical distribution clearly depicts that the vertical structure changes toward a top-heavy profile in both vertical motion and heating with a slight time lag as convection intensifies. This confirms that vertical motion and heating are tightly, although not perfectly, connected to each other throughout the evolution of the convective life cycle. The ω provided by ERA5 and the Q_1 provided by TRMM PR both exhibit a transition from shallow to deep convective and eventually to stratiform.

The THR is a measure proposed by BH17 for estimating the variability of vertical motion profiles. In this study, THR is applied to vertical pressure velocity and to diabatic heating to investigate the evolution of convective processes. The Q_1 THR reaches a peak at the time of peak precipitation or slightly after, followed several hours later by the ω THR. It is yet to be understood why vertical motion lags diabatic heating in the timing it develops from bottom-heavy to top-heavy profiles.

Furthermore, analysis of the regionality of the first and second EOF modes for both ω and Q_1 reveals that the first mode exhibits a coherent evolution without distinct regional variation. In contrast, the second mode demonstrates a transition of ω and Q_1 from shallow convection to stratiform convection, consistent with the typical lifecycle of MCS. Shallow convection remains persistent in the EP and AO regions, while diminishing during the convectively inactive phase in the WP and IO regions. When the two EOF modes of Q_1 are each decomposed into deep convective, stratiform, and shallow types, the first mode dominates in the deep convective Q_1 while the second mode takes the lead in the stratiform Q_1. In the case of shallow Q_1, both the first and second modes play comparable roles. There is no significant regional difference between the first and second modes when separated for the rain types.

The present work analyzes the regional characteristics of vertical motion and diabatic heating over tropical oceans with a focus on their vertical structure, as it influences large-scale circulation in diverse and significant ways (Back & Bretherton, 2006; Schumacher et al., 2004; Zhang & Hagos, 2009). More analysis to look into the

mechanisms linking vertical motion with diabatic heating and their regional dependence is worthy of further study by using high-resolution cloud-resolving models or improved observational data sets with finer temporal sampling in the future.

Data Availability Statement

GSMAP data were provided by the Japan Aerospace Exploration Agency (JAXA) (https://sharaku.eorc.jaxa.jp/GSMaP/). The TRMM data were obtained from NASA's Goddard Earth Sciences Data and Information Services Center (GES DISC) (https://disc.gsfc.nasa.gov/datasets/GPM_2HSLH_TRMM_07/summary?keywords=TRMM%20SLH). The CERES SYN1deg product is available from the CERES project of NASA Langley Atmospheric Science Data Center (https://ceres.larc.nasa.gov/data/#syn1deg-level-3). The ERA5 data sets are available from the European Center for Medium-Range Weather Forecast (ECMWF) website (https://www.ecmwf.int/en/forecasts/dataset/ecmwf-reanalysis-v5).

Acknowledgments
The work of YC is supported partly by the Institute for Space-Earth Environmental Research (ISEE) of Nagoya University and Japan-Taiwan Exchange Association.

References

Ahmed, F., Schumacher, C., & Feng, Z. (2016). Retrieval of latent heating from the 3D structure of precipitation. *Journal of Applied Meteorology and Climatology*, *55*(9), 1889–1905.

Back, L. E., & Bretherton, C. S. (2006). Geographic variability in the export of moist static energy and vertical motion profiles in the tropical Pacific. *Geophysical Research Letters*, *33*(17), L17810. https://doi.org/10.1029/2006gl026672

Back, L. E., & Bretherton, C. S. (2009). On the relationship between SST gradients, boundary layer winds, and convergence over the tropical oceans. *Journal of Climate*, *22*(15), 4182–4196. https://doi.org/10.1175/2009jcli2392.1

Back, L. E., Hansen, Z., & Handlos, Z. (2017). Estimating vertical motion profile top-heaviness: Reanalysis compared to satellite-based observations and stratiform rain fraction. *Journal of the Atmospheric Sciences*, *74*(3), 855–864. https://doi.org/10.1175/jas-d-16-0062.1

Barnes, H. C., Zuluaga, M. D., & Houze, R. A., Jr. (2015). Latent heating characteristics of the MJO computed from TRMM observations. *Journal of Geophysical Research: Atmospheres*, *120*(4), 1322–1334. https://doi.org/10.1002/2014jd022530

Berg, W., Kummerow, C., & Morales, C. A. (2002). Differences between east and west Pacific rainfall systems. *Journal of Climate*, *15*(24), 3659–3672. https://doi.org/10.1175/1520-0442(2002)015<3659:dbeawp>2.0.co;2

Bernardez, M., & Back, L. E. (2024). Integrating thermodynamic and dynamic views on the control of the top-heaviness of convection in the Pacific ITCZ with weak temperature gradient simulations. *Journal of Advances in Modeling Earth Systems*, *16*(2), e2022MS003455. https://doi.org/10.1029/2022ms003455

Bretherton, C. S., & Smolarkiewicz, P. K. (1989). Gravity waves, compensating subsidence and detrainment around cumulus clouds. *Journal of the Atmospheric Sciences*, *46*(6), 740–759. https://doi.org/10.1175/1520-0469(1989)046<0740:gwcsad>2.0.co;2

Bui, H. X., Yu, J.-Y., & Chou, C. (2016). Impacts of vertical structure of large-scale vertical motion in tropical climate: Moist static energy framework. *Journal of the Atmospheric Sciences*, *73*(11), 4427–4437. https://doi.org/10.1175/jas-d-16-0031.1

Chang, K.-W., & L'Ecuyer, T. S. (2019). Role of latent heating vertical distribution in the formation of the tropical cold trap. *Journal of Geophysical Research: Atmospheres*, *124*(14), 7836–7851. https://doi.org/10.1029/2018jd030194

Charney, J. G. (1963). A note on large-scale motions in the tropics. *Journal of the Atmospheric Sciences*, *20*(6), 607–609. https://doi.org/10.1175/1520-0469(1963)020<0607:anolsm>2.0.co;2

Chen, Y.-C., & Masunaga, H. (2024). The tropical convective evolution in different rain types over the West and East Pacific. *SOLA*, *20*, 392–399. https://doi.org/10.2151/sola.2024-052

Chen, Y.-C., & Yu, J.-Y. (2021). Modes of tropical convection and their roles in transporting moisture and moist static energy: Contrast between deep and shallow convection. *Climate Dynamics*, *57*(7–8), 1789–1803. https://doi.org/10.1007/s00382-021-05777-x

Chikira, M. (2014). A cumulus parameterization with state-dependent entrainment rate. Part II: Impact on climatology in a general circulation model. *Journal of the Atmospheric Sciences*, *71*(2), 615–639. https://doi.org/10.1175/jas-d-13-038.1

Doelling, D. R., Haney, C. O., Scarino, B. R., Gopalan, A., & Bhatt, R. (2016). Improvements to the geostationary visible imager ray-matching calibration algorithm for CERES edition 4. *Journal of Atmospheric and Oceanic Technology*, *33*(12), 2679–2698. https://doi.org/10.1175/jtech-d-16-0113.1

Doelling, D. R., Loeb, N., Keyes, D. F., Nordeen, M. L., Morstad, D., Wielicki, B. A., et al. (2013). Geostationary enhanced temporal interpolation for CERES flux products. *Journal of Atmospheric and Oceanic Technology*, *30*(6), 1072–1090. https://doi.org/10.1175/jtech-d-12-00136.1

Funk, A., Schumacher, C., & Awaka, J. (2013). Analysis of rain classifications over the tropics by version 7 of the TRMM PR 2A23 algorithm. *Journal of the Meteorological Society of Japan. Ser. II*, *91*(3), 257–272. https://doi.org/10.2151/jmsj.2013-302

Geisler, J. E. (1981). A linear model of the walker cell. *Journal of the Atmospheric Sciences*, *38*(7), 1390–1400. https://doi.org/10.1175/1520-0469(1981)038<1390:almotw>2.0.co;2

Hagos, S., Zhang, C., Tao, W.-K., Lang, S., Takayabu, Y. N., Shige, S., et al. (2010). Estimates of tropical diabatic heating profiles: Commonalities and uncertainties. *Journal of Climate*, *67*(3), 542–558. https://doi.org/10.1175/2009jcli3025.1

Handlos, Z. J., & Back, L. E. (2014). Estimating vertical motion profile shape within tropical weather states over the oceans. *Journal of Climate*, *27*(20), 7667–7686. https://doi.org/10.1175/jcli-d-13-00602.1

Hartmann, D., Hendon, H., & Houze, J. R. A. (1984). Some implications of the mesoscale circulations in cloud clusters for large-scale dynamics and climate. *Journal of the Atmospheric Sciences*, *41*(1), 113–121. https://doi.org/10.1175/1520-0469(1984)041<0113:siotmc>2.0.co;2

Hersbach, H., Bell, B., Berrisford, P., Hirahara, S., Horányi, A., Muñoz-Sabater, J., et al. (2020). The ERA5 global reanalysis. *The Quarterly Journal of the Royal Meteorological Society*, *146*(730), 1999–2049. https://doi.org/10.1002/qj.3803

Houze, R. A. (1989). Observed structure of mesoscale convective systems and implications for large-scale heating. *Journal of the Royal Meteorological Society*, *115*(487), 425–461. https://doi.org/10.1256/smsqj.48701

Houze, R. A. (1997). Stratiform precipitation in regions of convection: A meteorological paradox? *Bulletin America Meteorology Social*, *78*(10), 2179–2196. https://doi.org/10.1175/1520-0477(1997)078<2179:spiroc>2.0.co;2

Huaman, L., & Schumacher, C. (2018). Assessing the vertical latent heating structure of the east Pacific ITCZ using the CloudSat CPR and TRMM PR. *Journal of Climate*, *31*(7), 2563–2577. https://doi.org/10.1175/jcli-d-17-0590.1

Huaman, L., Schumacher, C., & Sobel, A. H. (2022). Assessing the vertical velocity of the east Pacific ITCZ. *Geophysical Research Letters*, *49*(1), e2021GL096192. https://doi.org/10.1029/2021gl096192

Inoue, K., & Back, L. E. (2015). Gross moist stability assessment during TOGA COARE: Various interpretations of gross moist stability. *Journal of the Atmospheric Sciences*, *72*(11), 4148–4166. https://doi.org/10.1175/jas-d-15-0092.1

Inoue, K., & Back, L. E. (2017). Gross moist stability analysis: Assessment of satellite-based products in the GMS plane. *Journal of the Atmospheric Sciences*, *74*(6), 1819–1837. https://doi.org/10.1175/jas-d-16-0218.1

Jiang, X., Waliser, D. E., Li, J.-L. F., Zhao, M., Olson, W. S., & Tao, W.-K. (2015). *Vertical diabatic heating structures of the MJO from TRMM and A-Train satellites*. Journal of Geophysical Research: Atmospheres (Vol. 120, pp. 3777–3798). https://journals.ametsoc.org/view/journals/mwre/139/10/2011mwr3636.1.pdf

Johnson, R. H., Rickenbach, T. M., Rutledge, S. A., Ciesielski, P. E., & Schubert, W. H. (1999). Trimodal characteristics of tropical convection. *Journal of Climate*, *12*(8), 2397–2418. https://doi.org/10.1175/1520-0442(1999)012<2397:tcotc>2.0.co;2

Kubar, T. L., Hartmann, D. L., & Wood, R. (2007). Radiative and convective driving of tropical high clouds. *Journal of Climate*, *20*(22), 5510–5526. https://doi.org/10.1175/2007jcli1628.1

Kubota, T., Aonashi, K., Ushio, T., Shige, S., Takayabu, Y. N., Kachi, M., et al. (2020). Global Satellite Mapping of Precipitation (GSMaP) products in the GPM era. *Advances in Global Change Research*, *67*, 355–373. https://doi.org/10.1007/978-3-030-24568-9_20

Kuo, Y.-H., Schiro, K. A., & Neelin, J. D. (2018). Convective transition statistics over tropical oceans for climate model diagnostics: Observational baseline. *Journal of the Atmospheric Sciences*, *75*(5), 1553–1570. https://doi.org/10.1175/jas-d-17-0287.1

Kurowski, M. J., Suselj, K., Grabowski, W. W., & Teixeira, T. (2018). Shallow-to-deep transition of continental moist convection: Cold pools, surface fluxes, and mesoscale organization. *Journal of the Atmospheric Sciences*, *75*(12), 4071–4090. https://doi.org/10.1175/jas-d-18-0031.1

Lamer, K., Kollias, P., & Nuijens, L. (2015). Observations of the variability of shallow trade wind cumulus cloudiness and mass flux. *Journal of Geophysical Research: Atmospheres*, *120*(12), 6161–6178. https://doi.org/10.1002/2014jd022950

Lappen, C.-L., & Schumacher, C. (2012). Heating in the tropical atmosphere: What level of detail is critical for accurate MJO simulations in GCMs? *Climate Dynamics*, *39*(9–10), 2547–2568. https://doi.org/10.1007/s00382-012-1327-y

Lappen, C.-L., & Schumacher, C. (2014). The role of tilted heating in the evolution of the MJO. *Journal of Geophysical Research: Atmospheres*, *119*(6), 2966–2989. https://doi.org/10.1002/2013jd020638

L'Ecuyer, T. S., & McGarragh, G. (2010). A ten-year climatology of tropical radiative heating and its vertical structure from TRMM observations. *Journal of Climate*, *23*(6), 1513–1525.

Ling, J. A., & Zhang, C. D. (2011). Structural evolution in heating profiles of the MJO in global reanalyses and TRMM retrievals. *Journal of Climate*, *24*(3), 825–842. https://doi.org/10.1175/2010jcli3826.1

Maloney, E. D., Gettelman, A., Ming, Y., Neelin, J. D., Barrie, D., & Mariotti, A. (2019). Process-oriented evaluation of climate and weather forecasting models. *Bulletin America Meteorology Social*, *100*, 1665–1686.

Mapes, B. E., & Houze, R. A., Jr. (1995). Diabatic divergence profiles in Western Pacific mesoscale convective systems. *Journal of the Atmospheric Sciences*, *52*(10), 1807–1828. https://doi.org/10.1175/1520-0469(1995)052<1807:ddpiwp>2.0.co;2

Mapes, B. E., Tulich, S., Lin, J., & Zuidema, P. (2006). The mesoscale convection life cycle: Building block or prototype for large-scale tropical waves? *Dynamics of Atmospheres and Oceans*, *42*(1–4), 3–29. https://doi.org/10.1016/j.dynatmoce.2006.03.003

Marinescu, P. J., van den Heever, S. C., Saleeby, S. M., Kreidenweis, S. M., & Posselt, D. J. (2016). The microphysical contributions to and evolution of latent heating profiles in two MC3E MCSs. *Journal of Geophysical Research: Atmospheres*, *121*(18), 10414–10436. https://doi.org/10.1002/2016jd024762

Masunaga, H. (2012). A satellite study of the atmospheric forcing and response to moist convection over tropical and subtropical oceans. *Journal of the Atmospheric Sciences*, *69*(1), 150–167. https://doi.org/10.1175/jas-d-11-016.1

Masunaga, H. (2013). A satellite study of tropical moist convection and environmental variability: A moisture and thermal budget analysis. *Journal of the Atmospheric Sciences*, *70*(8), 2443–2466. https://doi.org/10.1175/jas-d-12-0273.1

Masunaga, H., & L'Ecuyer, T. S. (2014). A mechanism of tropical convection inferred from observed variability in the moist static energy budget. *Journal of the Atmospheric Sciences*, *71*, 3747–3766.

Neelin, J. D., & Held, I. M. (1987). Modeling tropical convergence based on the moist static energy budget. *Monthly Weather Review*, *115*(1), 3–12. https://doi.org/10.1175/1520-0493(1987)115<0003:mtcbot>2.0.co;2

Nesbitt, S. W., Cifelli, R., & Rutledge, S. A. (2006). Storm morphology and rainfall characteristics of TRMM precipitation features. *Monthly Weather Review*, *134*(10), 2702–2721. https://doi.org/10.1175/mwr3200.1

Nesbitt, S. W., & Zipser, E. J. (2003). The diurnal cycle of rainfall and convective intensity according to three years of TRMM measurements. *Journal of Climate*, *16*(10), 1456–1475. https://doi.org/10.1175/1520-0442-16.10.1456

Powell, S. W., Houze, R. A., Jr., & Brodzik, S. R. (2016). Rainfall-type categorization of radar echoes using polar coordinate reflectivity data. *Journal of Atmospheric and Oceanic Technology*, *33*(3), 523–538. https://doi.org/10.1175/jtech-d-15-0135.1

Schumacher, C., Ciesielski, P. E., & Zhang, M. H. (2008). Tropical cloud heating profiles: Analysis from KWAJEX. *Monthly Weather Review*, *136*(11), 2593–2610. https://doi.org/10.1175/2008mwr2275.1

Schumacher, C., Houze, R. A., & Kraucunas, I. (2004). The tropical dynamical response to latent heating estimates derived from the TRMM precipitation radar. *Journal of the Atmospheric Sciences*, *61*(12), 1341–1358. https://doi.org/10.1175/1520-0469(2004)061<1341:ttdrtl>2.0.co;2

Schumacher, C., & Houze, R. A., Jr. (2003). Stratiform rain in the tropics as seen by the TRMM precipitation radar. *Journal of Climate*, *16*(11), 1739–1756. https://doi.org/10.1175/1520-0442(2003)016<1739:sritta>2.0.co;2

Sherwood, S. C., Bony, S., & Dufresne, J.-L. (2014). Spread in model climate sensitivity traced to atmospheric convective mixing. *Nature*, *505*(7481), 37–42. https://doi.org/10.1038/nature12829

Shige, S., Takayabu, Y. N., Kida, S., Tao, W.-K., Zeng, X., Yokoyama, C., & L'Ecuyer, T. (2009). Spectral retrieval of latent heating profiles from TRMM PR data. Part IV: Comparison of lookup tables from two- and three-dimensional cloud-resolving model simulations. *Journal of Climate*, *22*(20), 5577–5594. https://doi.org/10.1175/2009jcli2919.1

Shige, S., Takayabu, Y. N., Tao, W.-K., & Johnson, D. E. (2004). Spectral retrieval of latent heating profiles from TRMM PR data. Part I: Development of a model-based algorithm. *Journal of Applied Meteorology*, *43*(8), 1095–1113. https://doi.org/10.1175/1520-0450(2004)043<1095:srolhp>2.0.co;2

Shige, S., Takayabu, Y. N., Tao, W.-K., & Shie, C.-L. (2007). Spectral retrieval of latent heating profiles from TRMM PR data. Part II: Algorithm improvement and heating estimates over tropical ocean regions. *Journal of Applied Meteorology*, *46*(7), 1098–1124. https://doi.org/10.1175/jam2510.1

Sobel, A. H., & Bretherton, C. S. (2000). Modeling tropical precipitation in a single column. *Journal of Climate*, *13*(24), 4378–4392. https://doi.org/10.1175/1520-0442(2000)013<4378:mtpias>2.0.co;2

Takayabu, Y. N., Lau, K., & Sui, C. (1996). Observation of a quasi-2-day wave during TOGA COARE. *Monthly Weather Review*, *124*(9), 1892–1913. https://doi.org/10.1175/1520-0493(1996)124<1892:ooaqdw>2.0.co;2

Takayabu, Y. N., Shige, S., Tao, W.-K., & Hirota, N. (2010). Shallow and deep latent heating modes over tropical oceans observed with TRMM PR spectral latent heating data. *Journal of Climate*, *23*(8), 2030–2046. https://doi.org/10.1175/2009jcli3110.1

Tao, W.-K., Smith, E. A., Adler, R. F., Haddad, Z. S., Hou, A. Y., & Iguchi, T. (2006). Retrieval of latent heating from TRMM measurements. *Bulletin America Meteorology Social*, *87*, 1555–1572.

Trenberth, K. E., Stepaniak, D. P., & Caron, J. M. (2000). The global monsoon as seen through the divergent atmospheric circulation. *Journal of Climate*, *13*(22), 3969–3993. https://doi.org/10.1175/1520-0442(2000)013<3969:tgmast>2.0.co;2

Vogel, R., Nuijens, L., & Stevens, B. (2020). Influence of deepening and mesoscale organization of shallow convection on stratiform cloudiness in the downstream trades. *Quart. J. Roy. Meteor. Soc.*, *146*(726), 174–185. https://doi.org/10.1002/qj.3664

Wolding, B., Dias, J., Kiladis, G., Ahmed, F., Powell, S. W., Maloney, E., & Branson, M. (2020). Interactions between moisture and tropical convection. Part I: The coevolution of moisture and convection. *Journal of the Atmospheric Sciences*, *77*(5), 1783–1799. https://doi.org/10.1175/jas-d-19-0225.1

Wu, Z., Sarachik, E. S., & Battisti, D. S. (2000). Vertical structure of convective heating and the three-dimensional structure of the forced circulation on an equatorial beta plane. *Journal of the Atmospheric Sciences*, *57*(13), 2169–2187. https://doi.org/10.1175/1520-0469(2000)057<2169:vsocha>2.0.co;2

Xu, J., Ma, Z., Yan, S., & Peng, J. (2022). Do ERA5 and ERA5-land precipitation estimates outperform satellite-based precipitation products? A comprehensive comparison between state-of-the-art model-based and satellite-based precipitation products over mainland China. *Journal of Hydrology*, *605*, 127353. https://doi.org/10.1016/j.jhydrol.2021.127353

Yanai, M., Esbensen, S., & Chu, J.-H. (1973). Determination of bulk properties of tropical cloud clusters from large-scale heat and moisture budgets. *Journal of the Atmospheric Sciences*, *30*(4), 611–627. https://doi.org/10.1175/1520-0469(1973)030<0611:dobpot>2.0.co;2

Yokoyama, C., & Takayabu, Y. N. (2012). Relationships between rain characteristics and environment. Part I: TRMM precipitation features and the large-scale environment over the tropical Pacific. *Monthly Weather Review*, *140*(9), 2831–2840. https://doi.org/10.1175/mwr-d-11-00252.1

Zhang, C., & Hagos, S. M. (2009). Bi-modal structure and variability of large-scale diabatic heating in the tropics. *Journal of the Atmospheric Sciences*, *66*(12), 3621–3640. https://doi.org/10.1175/2009jas3089.1

Zhang, C., McGauley, M., & Bond, N. A. (2004). Shallow meridional circulation in the tropical eastern Pacific. *Journal of Climate*, *17*(1), 133–139. https://doi.org/10.1175/1520-0442(2004)017<0133:smcitt>2.0.co;2

Zhang, Y., & Klein, S. A. (2010). Mechanisms affecting the transition from shallow to deep convection over land: Inferences from observations of the diurnal cycle collected at the arm southern Great Plains site. *Journal of the Atmospheric Sciences*, *67*(9), 2943–2959. https://doi.org/10.1175/2010jas3366.1